International Journal of Heat and Technology
Vol. 44, No. 3, June, 2026, pp. 1091-1103
Journal homepage: http://iieta.org/journals/ijht

Integration of Evacuated Tube Collectors and Stratified Phase Change Material Storage in Solar Absorption Refrigeration: Annual Performance Assessment for Food Conservation

Mehdi Bendaoud*, Rabah Gomri

Department of HVAC Engineering, Faculty of Sciences and Technology, Climatic Engineering Laboratory, University Constantine 1, Constantine 25000, Algeria

Corresponding Author Email: mehdi.bendaoud@doc.umc.edu.dz

https://doi.org/10.18280/ijht.440317

Received: 13 April 2026
Revised: 10 June 2026
Accepted: 21 June 2026
Available online: 30 June 2026

Keywords:
energy performance, Evacuated Tube Collector, Hazard Analysis and Critical Control Points, LiBr–H_2O absorption, MATLAB modeling, Phase Change Material, solar refrigeration, thermal storage

ABSTRACT

This study evaluates the annual performance of a solar-assisted absorption refrigeration system designed for food preservation under the climatic conditions of Constantine, Algeria. The system combines an evacuated-tube collector field with integrated Phase Change Material (PCM), a stratified water–PCM storage tank, and a single-effect LiBr–H_2O absorption chiller, which supplies a 50 m³ cold room. A transient MATLAB model was developed using hourly meteorological data and a 60 s internal calculation step. Four configurations were compared under identical climatic, load, sizing, and control conditions: without PCM, PCM in the collectors only, PCM in the storage tank only, and PCM in both locations. The combined configuration achieved an annual thermal coefficient of performance (COP) of 0.727 and a generator-level solar fraction of 95.263%. The cold-room temperature remained between approximately 4.10 and 5.60 °C, providing 100% compliance with the selected product-specific storage interval of 3–8 °C. Compared with the PCM-free reference system, the combined arrangement increased the generator-level solar fraction by 0.626 percentage points, reduced unused solar heat by 1.65%, and lowered electrical backup consumption by 11.68%. The results indicate that PCM integration does not significantly modify the intrinsic COP or cooling capacity of the absorption chiller. Its principal contribution is to improve the temporal matching between solar-energy availability and generator demand, with the combined collector-and-tank arrangement providing the most favorable annual energy-management performance.

1. INTRODUCTION

Space cooling is a major and rapidly growing contributor to global electricity demand. According to the International Energy Agency, it accounted for approximately 9% of global final electricity consumption in 2022, and this demand could more than double by 2050 if no additional efficiency measures are implemented [1]. In the agri-food sector, reliable refrigeration is essential for limiting product deterioration and maintaining safe storage conditions. Solar-driven absorption cooling is therefore a promising alternative to conventional vapour-compression refrigeration, particularly in regions where high cooling demand coincides with abundant solar energy.

Single-effect LiBr–H_2O absorption chillers are suitable for solar thermal applications because they can be driven by moderate-temperature heat sources [2-5]. Coupling them with evacuated-tube collectors can provide the generator temperature required while limiting convective and conductive heat losses. Their vacuum insulation, selective absorber coatings, and compatibility with reflector-assisted configurations further support their use in medium-temperature solar applications [6, 7]. Nevertheless, annual performance remains sensitive to solar intermittency, Evacuated Tube Collector (ETC) area, storage capacity, and operating control. Insufficient collector area may increase auxiliary heating, whereas excessive sizing may generate substantial unused solar heat [3, 8, 9].

Phase Change Materials (PCM) provide an effective approach for reducing the temporal mismatch between solar-energy availability and cooling demand. Previous studies have investigated PCM-based thermal storage in solar cooling systems [10, 11] and the direct integration of PCM into evacuated-tube collectors [12]. Experimental studies have also shown that PCM location and inlet-flow configuration influence mixing and thermal stratification in hot-water storage tanks [13]. PCM effectiveness therefore depends not only on storage capacity, but also on phase-change temperature, mass, location, and compatibility with the operating temperature of the absorption chiller.

Complementary studies have addressed individual methodological and design aspects relevant to solar absorption cooling, including experimental validation, control, component sizing, and climate-dependent performance. Boero and Agyenim [8] validated a transient TRNSYS model against experimental measurements before applying it to different climates. Guerrero Delgado et al. [14] used long-term experimental data to validate a control-oriented model of a solar absorption cooling plant. Redpath et al. [9] examined collector and storage sizing under location-specific climatic conditions, while Sharma et al. [15] combined measured absorption-machine data with 2022 weather data to evaluate a solar absorption system with sensible thermal storage for milk chilling. These studies underline the importance of experimentally supported modelling, dynamic control, appropriate component sizing, and annual simulations reflecting local weather conditions.

However, the reviewed literature mainly treats collector-integrated PCM, PCM storage, tank stratification, sizing, and system control as separate design aspects. The cited studies do not provide a systematic four-case comparison isolating the individual and combined effects of PCM placed in the collectors and in a stratified storage tank under identical climatic, load, sizing, and control conditions. Moreover, the relationship between source-side energy management and the thermal performance of food-storage cold rooms remains insufficiently quantified for North African climates. The novelty of this work lies in a unified annual assessment that determines whether the two PCM locations provide independent, additive, or complementary benefits.

The present study develops a transient numerical model coupling evacuated-tube collectors, collector-level PCM, a multi-node stratified tank containing PCM, and a single-effect $LiBr–H_2O$ absorption chiller. Four configurations are evaluated using an hourly climatic dataset representative of Constantine, Algeria: a reference system without PCM, PCM in the collectors only, PCM in the storage tank only, and PCM at both levels. Their annual performance is compared in terms of coefficient of performance (COP), solar fraction at the generator level, auxiliary-energy consumption, and unused solar heat. The thermal response of a 50 m³ food-storage cold room is also assessed through compliance with the prescribed storage-temperature interval adopted for the selected application within a Hazard Analysis and Critical Control Points (HACCP)-oriented framework [16].

2. METHOD AND SYSTEM DESCRIPTION

2.1 System description

The studied solar-assisted refrigeration system (Figure 1) comprises four interconnected subsystems: an evacuated-tube collector field incorporating PCM, a vertically stratified water–PCM storage tank, a single-effect $LiBr–H_2O$ absorption machine, and a 50 m³ cold room. An electric resistance heater is installed in the generator loop as a backup source. Solar heat is prioritized, and the auxiliary heater supplies only the residual thermal demand when the storage temperature or available tank power is insufficient. The configuration is therefore treated as a solar-assisted hybrid absorption refrigeration system [17].

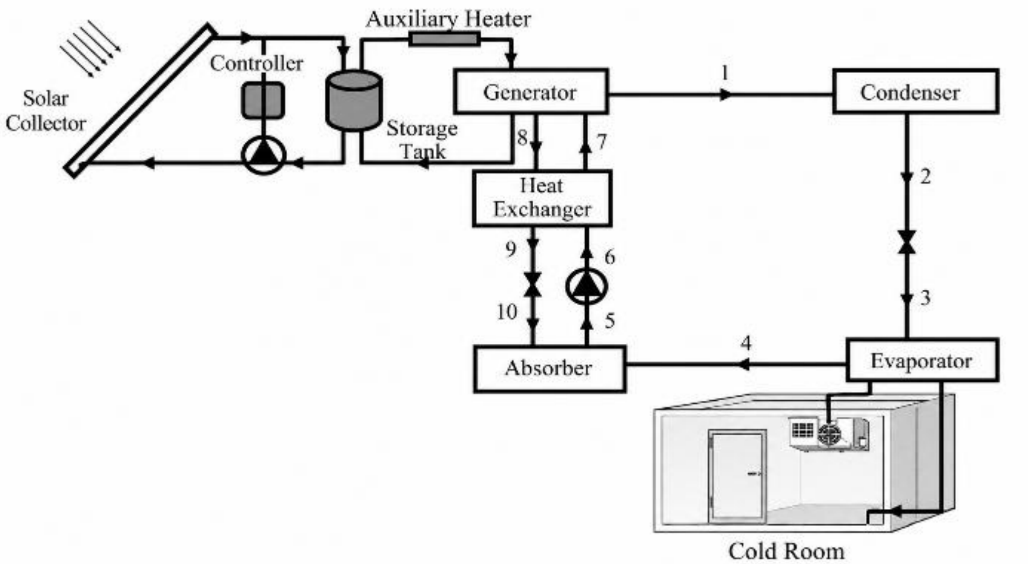

Figure 1. The schematic illustration of the solar absorption refrigeration system

2.1.1 Evacuated tube solar collectors

Retained collection surface: A_{coll} = 10 m²

Inclination and orientation: β = 35°, south-facing

Collector PCM: 15.9 kg of RT82 paraffin

PCM phase-change peak: T_{melt} = 82 ℃

PCM storage capacity: 170 kJ.kg^{-1} over the 70–85 ℃ interval

PCM specific heat: 2.0 kJ·kg^{-1}·K^{-1}

Solar-loop mass flow rate: 0.015 kg·m^{-2}·s^{-1} (0.150 kg·s^{-1})

Heat-transfer fluid: equivalent water–glycol mixture; c_p = 3.9 kJ·kg^{-1}·K^{-1}

Role: solar heat collection and short-term latent buffering; collector outlet temperature limited to 100 ℃. The selection of evacuated-tube collectors is supported by their ability to maintain comparatively high thermal performance at elevated operating temperatures, mainly because the vacuum envelope limits conductive and convective heat losses, while selective coatings improve solar-energy absorption [7].

The evacuated-tube collector model uses a nominal optical efficiency η_0 = 0.718 and thermal-loss coefficients a_1 = 1.36 W·m^{-2}·K^{-1}, and a_2 = 0.0025 W·m^{-2}·K^{-2} .These coefficients define the useful thermal output as a function of incident irradiance and the collector-to-ambient temperature difference, with the calculated efficiency bounded between 0 and 0.75. PCM integration absorbs part of the high-irradiance heat and delays its transfer when solar input decreases, thereby reducing short-term fluctuations in the temperature delivered to the tank [12, 18].

The RT82 phase change is represented by a continuous enthalpy formulation over a 3 K transition interval. The selected PCM mass provides approximately one hour of buffering equivalent to 15% of the nominal generator thermal power. Charging is enabled when the collector outlet reaches at least 85 °C, whereas discharge toward the tank requires a minimum positive temperature difference of 3 K [19].

2.1.2 Stratified storage tank

Total volume: V_{sto} = 700 L

Storage-to-collector ratio: 70 L/m²

Configuration: 20 fixed vertically stratified water nodes

Water mass: approximately 663 kg

Tank PCM: approximately 26.9 kg of RT82 (5% of tank volume)

PCM distribution: 70% in the upper 7 nodes, 30% in the middle 6 nodes, 0% in the lower 7 nodes

Overall heat-loss coefficient: U_{sto} = 0.35 $W \cdot m^{-2} \cdot K^{-1}$

Maximum storage temperature: 95 °C

Role: store solar heat and supply the absorption generator

The tank is represented by twenty equal fixed vertical nodes. Heat losses are evaluated for each node, and adjacent nodes exchange heat through an equivalent axial conductance accounting for water conduction, wall conduction, and residual mixing. The twenty-layer architecture and fourth-order Runge–Kutta basis are consistent with the model of Karlina et al. [20] and with validated one-dimensional multi-node storage models [21]. Solar heat is introduced at the thermally compatible level, with 90% supplied to that node and 10% to the immediately lower node. Hot water is withdrawn from the upper node for the generator, and the cooler return is reintroduced at a temperature-compatible level. A 60 s internal time step, a maximum Courant number of 0.35, and a conservative correction of adjacent inversions exceeding 0.10 K are used to limit artificial mixing.

The PCM is concentrated near the upper part of the tank to retain latent storage close to the generator operating temperature. The lower seven nodes contain no PCM so that a comparatively cool return can be maintained for the solar collectors. The adopted 70/30/0 distribution is a design assumption evaluated within the comparative cases: without PCM, collector PCM only, tank PCM only, and combined collector and tank PCM. The temperatures reported as upper, middle, and lower storage temperatures are representative outputs from the twenty-node field, not three computational zones [17].

2.1.3 LiBr–H_2O absorption machine

Type: single effect

Calculated peak cooling load for the reference Typical Meteorological Year (TMY): $\dot{Q}_{peak}$ = 2.65 kW

Design load (safety factor 1.15): $\dot{Q}_{design}$ = 3.05 kW

Selected nominal cooling capacity: $\dot{Q}_{cool,\ nom}$ = 3.50 kW

Nominal generator thermal power: $\dot{Q}_{gen,\ nom}$ = 5.00 kW

Evaporator temperature: T_{evap} = 0 °C; nominal condenser temperature: 35 °C

Generator temperature range: 75–95 °C; nominal value 90 °C; modeled condenser range: 28–45 °C

Nominal COP: 0.70

Minimum part-load ratio: 40%

Control: ON/OFF at 5.5 °C and 4.5 °C

The nominal machine capacity is derived automatically from the calculated cold-room load. For the reference Meteonorm TMY, a peak load of 2.65 kW becomes 3.05 kW after applying a 15% safety factor; the selected capacity is therefore 3.50 kW. Single-effect LiBr–H_2O machines are compatible with the medium-temperature heat supplied by evacuated-tube collectors [9, 10]. The working-pair properties are evaluated using established LiBr–H_2O formulations [22].

The instantaneous COP is adjusted according to generator, condenser, and evaporator temperatures and is limited to the range 0.62–0.75. The effective condenser temperature is estimated from the outdoor wet-bulb temperature with a 7 K cooling-tower approach and is bounded between 28 and 45 °C. The machine starts when the refrigerated-air temperature reaches 5.5 °C and stops at 4.5 °C, producing a 1 K hysteresis band around the 5 °C setpoint. During operation, the cooling output is not allowed to fall below 40% of nominal capacity; lower average loads are represented by cycling and the resulting duty cycle.

A 5.00 kW electric resistance heater, with an efficiency of 0.98, supplies only the generator heat not covered by the stratified tank. It is therefore a thermal backup for the absorption cycle and not a separate vapour-compression refrigeration unit. Solar generator input, auxiliary thermal input, auxiliary electricity, system auxiliaries, and unmet cooling demand are accounted for separately in the energy balance.

2.1.4 Cold room

Reference product: fresh oranges

Internal dimensions: 5.0 m × 4.0 m × 2.5 m

Volume: 50 m³

Target temperature: T_{target} = 5 °C

Selected product-specific evaluation interval: 3–8 °C

Air mass and specific heat: 60 kg; $c_{p,air}$ = 1005 $J \cdot kg^{-1} \cdot K^{-1}$

Stored product mass: 1500 kg; $c_{p,p}$ = 3400 $J \cdot kg^{-1} \cdot K^{-1}$

Daily product intake: 300 kg/day at 15 °C; $c_{p,in}$ = 3800 $J \cdot kg^{-1} \cdot K^{-1}$

Envelope surface and transmittance: A_{wall} = 85 m²; U_{wall} = 0.18 $W \cdot m^{-2} \cdot K^{-1}$

Air–product conductance: UA_{ap} = 45 $W \cdot K^{-1}$; added fast thermal capacitance: C_{fast} = 350 $kJ \cdot K^{-1}$

Fresh oranges are selected as the reference food product. The room setpoint is 5 °C, and 3–8 °C is used as a product-specific thermal-performance interval, consistent with postharvest guidance for oranges [23]. This interval must not be presented as a universal HACCP temperature band because Codex guidance requires product-specific hazards, critical limits, monitoring, and records rather than one temperature range for all fresh produce [24].

The cold room is represented by two coupled thermal nodes. The air-side node includes the heat capacity of 60 kg of air and an additional effective capacitance of 350 $kJ \cdot K^{-1}$representing internal surfaces, shelving, the evaporator, and rapidly responding parts of the stored load. The product node contains 1500 kg of oranges and exchanges heat with the air through an overall conductance of 45 $W \cdot K^{-1}$. Both nodes are initialized at 5 °C.

The refrigeration load includes envelope transmission, permanent leakage, door-opening infiltration, sensible and latent infiltration loads, incoming-product cooling, lighting, occupants, evaporator-fan heat, and a 40 W product respiration gain. For the reference Meteonorm TMY, the resulting peak load of 2.65 kW provides the basis for selecting the 3.50 kW absorption unit. Because the peak is calculated from the meteorological input, these two values must be updated if the TMY file or operating assumptions are changed. The adopted effective capacitance, conductance, and biological-load parameters are retained as model assumptions and should be examined through sensitivity analysis and future experimental calibration [25, 26].

2.2 Mathematical modeling

The mathematical model was developed to describe the main thermal and energy interactions within the proposed solar-assisted refrigeration system. It includes a two-node representation of the refrigerated room, an evacuated-tube solar collector field, PCM, a vertically stratified water–PCM storage tank, and a single-effect LiBr–H_2O absorption chiller. The governing equations are formulated from mass and energy conservation principles and are coupled through the heat-transfer rates exchanged between the different subsystems.

2.2.1 Two-node cold-room model

The refrigerated air and the stored products are represented by two interacting thermal nodes. Their energy balances are written as:

$$C_{\mathrm{air}}\frac{\mathrm{d}T_{\mathrm{air}}}{\mathrm{d}t} = \dot{Q}_{\mathrm{ext}} + UA_{\mathrm{ap}}\left(T_{\mathrm{p}} - T_{\mathrm{air}}\right) - \dot{Q}_{cool} \tag{1}$$

$$C_{\mathrm{p}}\frac{\mathrm{d}T_{\mathrm{p}}}{\mathrm{d}t} = UA_{\mathrm{ap}}\left(T_{\mathrm{air}} - T_{\mathrm{p}}\right) \tag{2}$$

The effective thermal capacitances of the air-side node and the product node are

$$C_{\mathrm{air}} = m_{\mathrm{air}}c_{p,\mathrm{air}} + C_{\mathrm{fast}}, C_{\mathrm{p}} = m_{\mathrm{p}}c_{p,\mathrm{p}} \tag{3}$$

The total thermal load applied to the air node is decomposed into transmission, permanent air leakage, door-opening infiltration, incoming-product, and internal contributions:

$$\dot{Q}_{\mathrm{ext}} = \dot{Q}_{\mathrm{tr}} + \dot{Q}_{\mathrm{leak}} + \dot{Q}_{\mathrm{door}} + \dot{Q}_{\mathrm{prod}} + \dot{Q}_{\mathrm{int}} \tag{4}$$

where, UA_{ap} is the overall air-product conductance, C_{fast} represents the rapidly responding internal thermal mass, and $\dot{Q}_{\mathrm{cool}}$ is the cooling power supplied by the absorption machine. The leakage and door-opening terms each include their sensible and latent components

2.2.2 Solar collector modelling

The useful thermal power delivered by the solar collector field is calculated as:

$$\dot{Q}_{solar} = \eta_{\mathrm{coll}}\, A_{\mathrm{coll}}\, G_{\beta} \tag{5}$$

where, η_{coll} is the instantaneous collector efficiency, A_{coll} is the total collector area, and G_β is the total solar irradiance incident on the tilted collector surface.

The instantaneous collector efficiency varies with the operating conditions and is determined from the quadratic performance correlation:

$$\eta_{\mathrm{coll}} = \eta_0 - a_1\frac{(T_{\mathrm{m}} - T_{\mathrm{ext}})}{G_\beta} - a_2\frac{(T_{\mathrm{m}} - T_{\mathrm{ext}})^2}{G_\beta} \tag{6}$$

where, η_0 is the optical efficiency, a_1 and a_2 are the first- and second-order heat-loss coefficients, respectively, T_{ext} is the ambient temperature, and T_{m} is the mean fluid temperature inside the collector.

The mean fluid temperature is defined as:

$$T_{\mathrm{m}} = \frac{T_{\mathrm{in}} + T_{\mathrm{out}}}{2} \tag{7}$$

where, T_{in} and T_{out} denote the collector inlet and outlet fluid temperatures, respectively.

2.2.3 Phase Change Material enthalpy formulation

For each storage node i, the total sensible and latent energy of water and PCM is represented by the nodal enthalpy:

$$H_i = \left(m_{\mathrm{w},i}c_{p,\mathrm{w}} + m_{\mathrm{pcm},i}c_{p,\mathrm{pcm},i}\right)(T_i - T_{\mathrm{ref}}) + m_{\mathrm{pcm},i}L_{\mathrm{pcm},i}f_i \tag{8}$$

The liquid fraction varies continuously within the phase-change interval:

$$f_i = \begin{cases} 0, & T_i \le T_{\mathrm{fus},i} - \Delta T_{\mathrm{fus}}, \\ \dfrac{T_i - \left(T_{\mathrm{fus},i} - \Delta T_{\mathrm{fus}}\right)}{\Delta T_{\mathrm{fus}}}, & T_{\mathrm{fus},i} - \Delta T_{\mathrm{fus}} < T_i < T_{\mathrm{fus},i}, \\ 1, & T_i \ge T_{\mathrm{fus},i}. \end{cases} \tag{9}$$

where, H_i is a nodal energy expressed in joules, while $f_i = 0$ and $f_i = 1$ correspond to the fully solid and fully liquid states, respectively.

2.2.4 Stratified water-Phase Change Material storage tank

The tank is discretized into 20 fixed vertical nodes. The enthalpy balance of node i is:

$$\frac{\mathrm{d}H_i}{\mathrm{d}t} = \dot{Q}_{\mathrm{hyd},i} + \dot{Q}_{i-1,i} - \dot{Q}_{i,i+1} - \dot{Q}_{\mathrm{loss},i} \tag{10}$$

The axial heat transfer between adjacent nodes and the thermal loss to the surroundings are expressed as:

$$\dot{Q}_{i,i+1} = UA_{\mathrm{inter}}(T_i - T_{i+1}) \tag{11}$$

$$\dot{Q}_{\mathrm{loss},i} = U_{\mathrm{tank}}\frac{A_{\mathrm{tank}}}{N_{\mathrm{nodes}}}\max(0, T_i - T_{\mathrm{ext}}) \tag{12}$$

where, $\dot{Q}_{\mathrm{hyd},i}$ is the signed hydraulic power associated with charging, thermal-energy withdrawal by the absorption-machine generator, and return-flow reinjection, whereas UA_{inter} governs heat transfer between adjacent layers.

2.2.5 Absorption machine and auxiliary heater

The single-effect absorption machine is described by a thermal COP. Before applying the capacity and control constraints, the cooling potential associated with the thermal power supplied to the generator is

$$\dot{Q}_{cool,th} = COP \times \dot{Q}_{gen,total} \tag{13}$$

The cooling capacity under the prevailing generator and condenser temperatures is corrected by the dimensionless factor f_{cap}:

$$\dot{Q}_{cap,avail} = f_{cap} \times \dot{Q}_{cool,nom} \tag{14}$$

The cooling demand is limited to the capacity available at the current operating conditions:

$$\dot{Q}_{cool,cmd} = min\left(\dot{Q}_{cool,req}, \dot{Q}_{cap,avail} \right) \tag{15}$$

The machine is operated only when $\dot{Q}_{cool,cmd} \geq PLR_{min} \dot{Q}_{cool,nom}$; otherwise, it is switched off and the commanded cooling power is set to zero.

During operation, the part-load ratio, the bounded COP, and the corresponding generator demand are evaluated as

$$PLR = \frac{\dot{Q}_{cool,cmd}}{\dot{Q}_{cool,nom}} \tag{16}$$

$$COP = min[COP_{max}, max(COP_{min}, COP_{base}(0.94 + 0.06\, PLR))] \tag{17}$$

$$\dot{Q}_{gen,req} = \frac{\dot{Q}_{cool,cmd}}{COP} \tag{18}$$

Eq. (17) restricts the calculated COP to the interval from COP_{min} to COP_{max} and replaces the programming-specific clip operator with standard minimum and maximum functions.

Solar heat is used first, while the auxiliary heater supplies only the remaining generator demand:

$$\dot{Q}_{gen,total} = \dot{Q}_{gen,solar} + \dot{Q}_{aux} \tag{19}$$

$$\dot{Q}_{aux} = \min[\dot{Q}_{aux,nom}, \max(0, \dot{Q}_{gen,req} - \dot{Q}_{gen,solar})] \tag{20}$$

The cooling power actually delivered is limited by both the command and the thermal power effectively available at the generator:

$$\dot{Q}_{cool} = min\left[\dot{Q}_{cool,cmd}, COP\left(\dot{Q}_{gen,solar} + \dot{Q}_{aux}\right)\right] \tag{21}$$

This formulation gives priority to solar energy, prevents operation below the admissible part-load range, and accounts explicitly for the nominal limit of the auxiliary heater.

2.2.6 Performance indicators

The thermal annual COP, based exclusively on the thermal energy supplied to the absorption generator, is:

$$COP_{\text{th,annual}} = \frac{E_{\text{cool}}}{E_{\text{gen,total}}} \tag{22}$$

The conventional thermal solar fraction at the generator is:

$$SF_{\text{th}} = 100\, \frac{E_{\text{gen,solar}}}{E_{\text{gen,total}}} \tag{23}$$

The fraction of the useful solar energy collected by the field that is effectively transferred to the generator is:

$$\eta_{\text{solar,use}} = 100\, \frac{E_{\text{gen,solar}}}{E_{\text{solar}}} \tag{24}$$

Cold-room temperature compliance is evaluated over the product-specific admissible interval of 3–8 °C:

$$R_{3\text{-}8} = \frac{100}{N} \sum_{k=1}^{N} I\left(3 \leq T_{\text{air,k}} \leq 8\right) \tag{25}$$

where, $T_{\text{air},k}$ is the cold-room air temperature at time step k, and N is the total number of evaluated hourly time steps. For a non-leap-year annual simulation, $N = 8760$.

2.3 Simulation algorithm

The annual simulation was performed in MATLAB using hourly Meteonorm data, with each hour divided into 60 internal steps of 60 s. At each time step, the model calculates the collector thermal output, updates the collector PCM and the 20-node stratified storage tank, evaluates the cold-room thermal loads, controls the absorption machine, and determines the solar and auxiliary heat supplied to the generator. The cold-room air and product temperatures, as well as the continuous storage states, are integrated using the fourth-order Runge–Kutta method. Hydraulic flows, PCM charging and discharging, and ON/OFF switching are handled through conservative operator splitting. The main temperatures, energy flows, COP, operating time, solar fraction, and unmet cooling demand are then stored for annual performance analysis.

3. RESULTS AND DISCUSSION

3.1 Contextual comparison with the literature

Table 1 compares the performance of the present system with selected studies.

To evaluate the physical consistency of the developed model and position the proposed configuration relative to existing solar-driven cooling technologies, its main performance indicators were compared with values reported in the literature, as summarized in Table 1. The annual thermal COP of the absorption chiller reached 0.727. This value is higher than the average COP of 0.679 reported by Zhu et al. [27] for a PCM-assisted absorption cooling configuration and is close to the single-effect COP range of 0.67–0.72 reported by Li et al. [28]. It also falls within the range generally expected for single-effect LiBr–H_2O absorption systems operating under suitable generator and heat-rejection conditions. Although the reference studies were conducted under different climatic conditions, operating periods, cooling-load profiles, system configurations, and control strategies, the agreement in COP supports the thermodynamic consistency of the proposed model.

A more pronounced difference was observed in the thermal solar fraction. The generator-level solar fraction reached 95.263%, which is numerically higher than the values of 74.5%, approximately 58%, and 71.99% reported by Al-Falahi et al. [3], Mehmood et al. [11], and Li et al. [28], respectively. The comparison with Mehmood et al. [11] is the most relevant because, according to the reported indicator definitions, both solar fractions represent the contribution of solar heat relative to the combined solar and auxiliary thermal energy supplied to the refrigeration system. The comparisons with Al-Falahi et al. [3] and Li et al. [28] should be regarded as indicative rather than strictly quantitative because of differences in climatic conditions, operating periods, system boundaries, and absorption-cycle configurations. The comparatively high solar fraction obtained in the present study can be associated with the combined use of PCM in the collector field, stratified water–PCM thermal storage, and an operating strategy that improves the availability of useful heat at the generator. Nevertheless, this result should not be attributed to PCM alone, since collector sizing, storage capacity, climatic conditions, and auxiliary-heating control also influence the annual solar contribution.

Table 1. Comparison of the present study with existing research

Reference	System Configuration and Application	Assessment Period	Reported COP	Thermal Solar Fraction
Al-Falahi et al. [3]	Single-effect LiBr–H_2O absorption system driven by ETC and auxiliary heating; building cooling	Cooling season	0.44 seasonal; 0.39–0.52 monthly	Approximately 58% seasonal
Mehmood et al. [11]	ETC-driven absorption cooling with latent-heat storage and auxiliary heating; residential cooling	Annual simulation	NR as a comparable annual value	74.5% with PCM; 70.3% with water storage
Zhu et al. [27]	PCM-assisted solar absorption cooling system	Selected operating periods	0.679 average with PCM	NR
Li et al. [28]	Solar single/double-effect switching LiBr–H_2O system with auxiliary heating; building cooling	June–September	0.67–0.72 in single-effect mode	71.99% over the cooling season
Mostafa et al. [29]	Solar-assisted adsorption refrigeration for a cold store	Annual simulation	NR as a single annual value	79% annual
Alammar et al. [30]	ETC-driven adsorption refrigeration with thermal storage; 38 m³ food cold store	8760 h annual simulation	0.47–0.60	95–100% for selected configurations
Present study	Single-effect LiBr–H_2O absorption with ETC, collector PCM, stratified water–PCM storage and electrical backup; 50 m³ cold room	8760 h annual dynamic simulation	0.727 annual thermal COP	95.263% at the generator

Note: Phase Change Material (PCM); Coefficient of performance (COP).

From an application perspective, Mostafa et al. [29] and Alammar et al. [30] also investigated annual solar-driven cold-storage systems. Mostafa et al. [29] reported an annual solar fraction of 79%, whereas Alammar et al. [30] obtained values between 95% and 100% for selected combinations of collector area and storage volume. However, both studies employed adsorption refrigeration rather than LiBr–H_2O absorption, and the solar fraction reported by Alammar et al. [30] was based on the ratio of useful collector energy to the thermal demand of the hot-water loop. These results are therefore useful for application-level contextualization but are not directly equivalent to the generator-level thermal solar fraction adopted in the present study.

With the contribution of the electrical backup, the annual cooling demand was fully met, and the cold-room temperature remained within the prescribed interval throughout the simulated year, corresponding to an annual temperature-compliance rate of 100%. This result characterizes the performance of the complete hybrid system rather than the autonomous performance of the solar subsystem. The compliance indicator nevertheless provides a useful application-oriented assessment because most comparable cold-storage studies reported temperature profiles or set-point maintenance without quantifying the proportion of annual hours within a predefined acceptable temperature range.

3.2 Evaluation of thermodynamic and temperature-control performance

Table 1 shows the present results with representative solar-driven refrigeration systems reported in the literature. The annual thermal COP obtained in this study was 0.727. This value is higher than the average COP of 0.679 reported by Zhu et al. [27] for a PCM-assisted absorption system and the seasonal COP of 0.44 reported by Al-Falahi et al. [3]. It is also close to the single-effect COP range of 0.67–0.72 reported by Li et al. [28]. However, these differences should be interpreted with caution because the studies were conducted under different climatic conditions, assessment periods, load profiles, storage configurations, and control strategies.

The generator-level thermal solar fraction reached 95.263%, with the auxiliary heater supplying the remaining 4.7% of the generator demand. This value was higher than the 74.5% reported by Mehmood et al. [11], the approximately 58% obtained by Al-Falahi et al. [3], the 71.99% reported by Li et al. [28], and the 79% obtained by Mostafa et al. [29]. Alammar et al. [30] reported comparable values of 95–100% for selected configurations; nevertheless, their system employed adsorption refrigeration and adopted a different definition of solar contribution. Therefore, the reported values are useful for contextual comparison but are not strictly equivalent. The generator-level thermal solar fraction characterizes only the thermal energy supplied to the absorption-machine generator and should not be interpreted as complete energy autonomy of the overall system.

The proposed system maintained the cold-room air temperature between 4.10 and 5.60 °C throughout the annual simulation, resulting in complete compliance with the selected preservation-temperature range. The modeled unmet cooling demand was zero; the 0.003 MWh year^{-1} difference reported in Table 3 was treated as a numerical energy-balance residual associated with time integration and rounding.

The absorption unit operated for 3018 h year^{-1}, while the stratified tank maintained average temperatures of 87.36, 84.50, and 80.62 °C in its upper, middle, and lower regions, respectively. These temperatures remained compatible with the operating requirements of a single-effect LiBr–H_2O absorption machine. The ordered annual regional mean temperatures indicate that the average vertical stratification was satisfactorily preserved.

The PCM components underwent repeated charging and discharging cycles, with approximately 96 equivalent annual cycles calculated for the tank PCM. This behavior is consistent with the thermal-buffering function generally attributed to

PCM integration in evacuated-tube collectors and solar cooling storage systems [12, 15, 31]. Nevertheless, the specific contribution of PCM is quantified through the four-case comparison presented in Section 3.7 with an otherwise identical configuration operating without latent storage.

Of the 10.55 MWh of annual solar energy collected, 6.48 MWh was delivered to the generator, corresponding to a solar-energy utilization ratio of 61.4%, while approximately 3.11 MWh was rejected or curtailed. This result indicates a temporal mismatch between solar availability, storage acceptance, and generator demand rather than inadequate collector performance. Consequently, further optimization should focus on collector–storage matching, control strategy, and auxiliary-energy reduction rather than increasing the nominal cooling capacity.

Overall, the results supported the thermodynamic feasibility of the proposed configuration under the simulated climatic and operating conditions. Temperature compliance is an important indicator for cold-chain performance [32, 33], but it should not be presented as complete HACCP certification. Nevertheless, experimental validation, sensitivity analysis, and economic assessment remain necessary to establish the practical benefit of the proposed storage configuration.

3.3 Global performance assessment of the system

The overall performance of the proposed system was evaluated using the annual thermal COP, solar contribution, operating duration, and cold-room temperature compliance. The annual thermal COP reached 0.727, while the time-weighted COP during machine operation was 0.726. These values are consistent with the typical performance range of single-effect LiBr–H_2O absorption systems reported in previous studies [2-5].

The generator-level thermal solar fraction was 95.263%, indicating that solar energy supplied most of the generator heat demand, whereas the auxiliary heater contributed the remaining 4.7%. This generator-level indicator excludes the electricity consumed by the backup heater and auxiliary components and should therefore not be interpreted as complete system energy autonomy.

The absorption machine operated for 3018 h year^{-1}, corresponding to approximately 34.5% of the annual period. Despite this moderate operating duration, the system satisfied the calculated cooling demand within the numerical tolerance of the annual simulation and maintained the cold-room air temperature between 4.10 and 5.60 °C, with no temperature excursions outside the selected 3–8 °C range.

These results indicated that, under the simulated conditions and with auxiliary heating available, the proposed configuration maintained the selected 3–8 ℃ temperature interval while relying predominantly on solar thermal energy. Nevertheless, this temperature-compliance indicator represents thermal conformity with the selected preservation range rather than complete HACCP certification.

3.4 Annual energy balance and system efficiency

Figure 2 illustrates the annual evolution of the absorption chiller operating COP relative to its nominal value and the prescribed minimum and maximum limits.

The COP remained stable throughout the year, with values generally ranging from 0.72 to 0.74 and an annual average close to 0.727. The limited fluctuations reflect seasonal variations in generator temperature and solar energy availability. Overall, the absorption chiller operates within a favourable and consistent performance range.

Figure 3 presents the monthly energy balance of the system, including the solar energy collected, the thermal energy supplied to the generator, and the resulting cooling production.

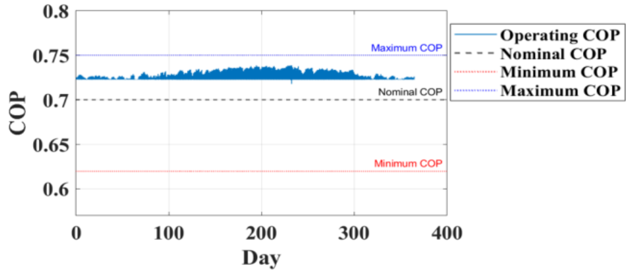

Figure 2. Coefficient of performance (COP) distribution

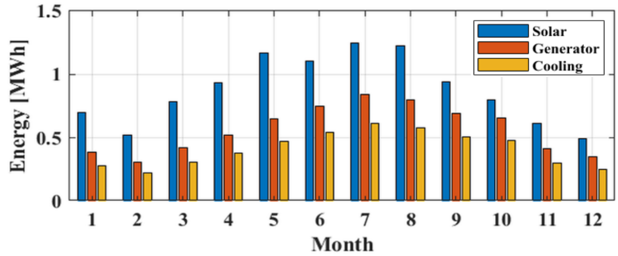

Figure 3. Monthly energy balances

Table 2 shows the monthly variations in collected solar energy, cooling energy produced, and average outdoor temperature, highlighting the seasonal behavior of the system.

Table 2. Monthly balances

Month	E_{solar} [MWh]	$E_{gen,total}$ [MWh]	E_{cool} [MWh]	$T_{ext,avg}$ [°C]
January	0.702	0.384	0.284	7.2
February	0.522	0.303	0.223	7.8
March	0.782	0.425	0.305	10.6
April	0.933	0.526	0.376	13.3
May	1.173	0.647	0.467	17.8
June	1.103	0.758	0.549	22.8
July	1.254	0.849	0.610	26.1
August	1.224	0.799	0.589	26.1
September	0.933	0.698	0.508	22.2
October	0.802	0.657	0.477	17.8
November	0.622	0.415	0.305	12.2
December	0.501	0.344	0.254	8.3

Table 3 summarizes the annual energy balance and the main performance indicators of the simulated solar absorption cooling system, including energy flows, COP values, solar contribution, operating time, and temperature compliance.

The three energy flows followed the same seasonal pattern, increasing from winter to a maximum in July before decreasing toward the end of the year. Cooling production remained consistently proportional to the generator input, indicating stable absorption-chiller performance, while the difference between these two quantities reflected the expected COP below unity. At the monthly scale, the collected solar energy exceeded the generator demand throughout the year, although this comparison did not capture possible short-term mismatches between solar availability and cooling demand.

Table 3. Annual energy balance

Indicator	Annual Value	Daily Average
Solar energy captured by the collectors, $\boldsymbol{E}_{\mathbf{solar}}$	10.551 MWh year⁻¹	28.91 kWh·day⁻¹
Solar heat supplied to the generator	6.483 MWh year⁻¹	17.76 kWh·day⁻¹
Auxiliary thermal input	0.322 MWh year⁻¹	0.88 kWh·day⁻¹
Total generator thermal input, $\boldsymbol{E}_{\mathbf{gen,total}}$	6.805 MWh year⁻¹	18.64 kWh·day⁻¹
Cooling energy produced, $\boldsymbol{E}_{\mathbf{cool}}$	4.947 MWh year⁻¹	13.55 kWh·day⁻¹
External cold-room cooling load	4.950 MWh year⁻¹	13.56 kWh·day⁻¹
Stratified storage-tank thermal losses	0.963 MWh year⁻¹	2.64 kWh·day⁻¹
Annual thermal COP, $\boldsymbol{E}_{\mathbf{cool}}/\boldsymbol{E}_{\mathbf{gen,total}}$	0.727	-
Mean COP during operation	0.726	-
Generator-level thermal solar fraction	95.263%	-
Temperature compliance within 3-8 °C	100.0%	-
Absorption-machine operating time	3018 h·year⁻¹ (34.5%)	8.27 h·day⁻¹
Equivalent full-load operating time	1413 h·year⁻¹	3.87 h·day⁻¹

Note: The difference of 0.003 MWh·year⁻¹ between the annual external cooling load and the cooling energy produced is a negligible numerical energy-balance residual, corresponding to approximately 0.06% of the annual cooling load, and is within the numerical tolerance associated with time integration and rounding. The calculated unmet cooling demand was zero.

3.5 Thermal behavior of solar collectors and Phase Change Material storage

3.5.1 Stratified tank

Figures 4-6 present the annual daily statistics of the stratified-tank temperature in the lower, middle, and upper regions, respectively.

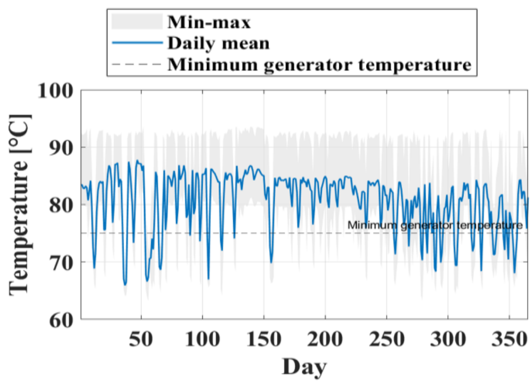

Figure 4. Stratified-tank temperature in the lower region

The temperature level increased progressively from the lower region to the top of the tank, confirming that thermal stratification was maintained throughout most of the year. Despite recurrent short-term drops, the daily mean temperatures remained generally within approximately 80–92 °C, indicating that the storage system effectively buffered variations in solar input and generator demand. The larger fluctuations observed during certain periods, particularly toward the end of the year, suggested temporary depletion caused by successive thermal withdrawals or reduced solar availability rather than a sustained loss of storage capacity. In the upper region, the top-node temperature remained slightly higher than the regional mean and exceeded the 75 °C generator threshold during most operating days. However, occasional crossings below this limit might interrupt or restrict chiller operation, highlighting the importance of using the top-node temperature, rather than the average tank temperature alone, in the generator control strategy.

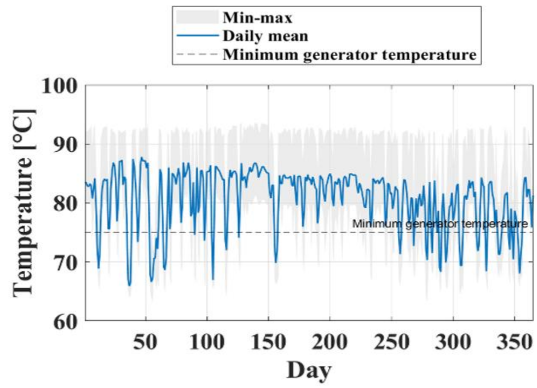

Figure 5. Stratified-tank temperature in the middle region

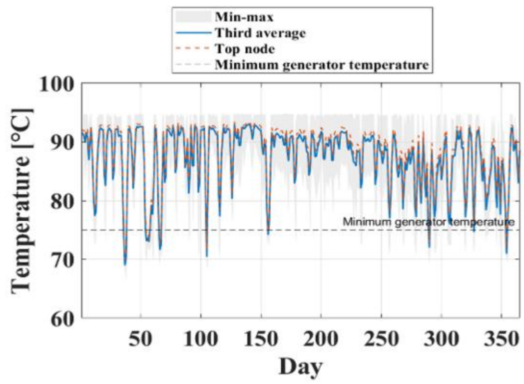

Figure 6. Stratified-tank temperature in the upper region

3.5.2 Solar collectors with Phase Change Material

Figure 7 presents the annual variation in the liquid fraction of the PCM integrated into the solar collector.

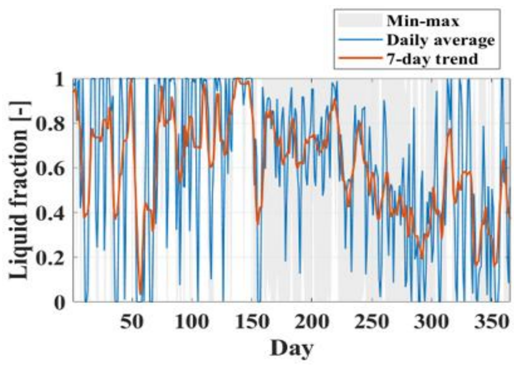

Figure 7. Annual evolution of the collector- Phase Change Material (PCM) liquid fraction

The PCM undergoes repeated melting and solidification cycles, confirming its active role in thermal storage. The higher liquid fractions observed during sunny periods indicated effective charging, while the lower values reflected heat release during reduced solar availability. Overall, the PCM contributes to smoothing short-term thermal fluctuations in the collector.

3.5.3 Collector efficiency

Figure 8 illustrates the daily mean collector efficiency and its 7-day moving average throughout the annual simulation.

The collector efficiency remained within a relatively stable range of 45–55%, while the moving average indicated only limited seasonal variation throughout the year. The highest and most consistent values were recorded during the middle months, coinciding with improved solar irradiance and more favourable thermal operating conditions. The sharp daily reductions, particularly toward the end of the year, might have been associated with temporary decreases in solar irradiance, elevated collector inlet-fluid temperatures, or shorter effective operating periods. However, identifying the direct cause required comparing these reductions with the corresponding irradiance, inlet-temperature, and flow-rate data. Overall, the smoothed trend confirmed that the collector maintained stable and satisfactory annual thermal performance despite short-term climatic fluctuations.

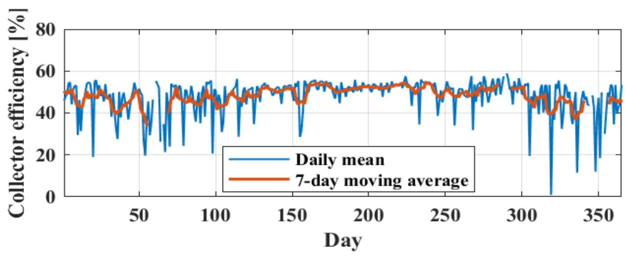

Figure 8. Daily mean collector efficiency and 7-day moving average

3.6 Thermal performance of the cold room

Figure 9 presents the annual frequency distribution of the hourly cold-room air temperature relative to the prescribed operating limits of 3 and 8 °C.

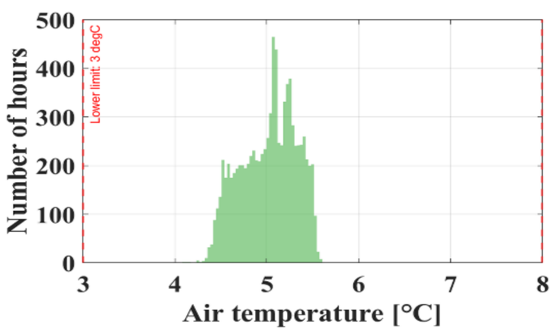

Figure 9. Annual frequency distribution of hourly cold-room air temperature

The temperature distribution was strongly concentrated around the 5 °C setpoint, with most hourly values occurring between approximately 4.5 and 5.5 °C. All represented temperatures remained well within the prescribed 3–8 °C interval, with no apparent occurrence of either undercooling or overheating. The narrow and nearly centred distribution indicated effective temperature regulation and sufficient thermal buffering against variations in ambient conditions and cooling demand. The limited dispersion around the setpoint might mainly result from the ON/OFF control hysteresis and the thermal inertia of the refrigerated enclosure rather than from a sustained loss of system performance.

3.6.1 Thermal statistics

Figure 10 presents the annual evolution of the daily mean cold-room air and product temperatures, together with the daily air-temperature range and the selected limits of 3 and 8 °C.

Both temperatures remained closely centred around the 5 °C setpoint throughout the year. The air temperature exhibited small short-term fluctuations, whereas the product temperature followed a smoother profile because of its greater thermal inertia. Moreover, the daily air-temperature envelope remains approximately between 4.2 and 5.6 °C and did not approach either regulatory limit. This limited dispersion indicated stable temperature control and effective attenuation of daily thermal disturbances. The slightly larger variations observed during a few isolated periods are temporary and did not suggest any persistent deterioration in cooling performance. Overall, the simulation indicated temperature conformity with the selected 3–8 °C interval for fresh oranges, with no simulated overheating or excessive cooling during the assessed year.

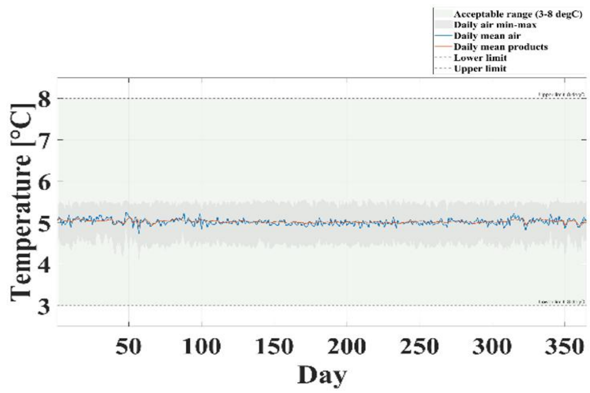

Figure 10. Annual cold-room air and product temperature profiles

3.7 Comparative assessment of collector and tank Phase Change Material configurations

Table 4 compares the four PCM configurations in terms of solar fraction at the generator level, unused solar heat, and electrical backup consumption, thereby quantifying the individual and combined contributions of PCM integration in the collectors and storage tank.

The four-case comparison indicates that PCM integration primarily affects the management of solar thermal energy supplied to the generator rather than the intrinsic performance of the absorption chiller. The annual COP, operating COP, cooling production, operating duration, and compliance with the prescribed 3–8 °C temperature range remain practically unchanged across the four configurations. This stability is expected because the same cooling load, chiller performance model, control strategy, and operating conditions were applied in all simulations. Therefore, the observed differences can mainly be attributed to changes in solar heat storage, recovery, and substitution of electrical backup heating.

When PCM is integrated only into the solar collectors, the solar fraction at the generator level increases from 94.637% to 94.979%, corresponding to a gain of 0.342 percentage points. At the same time, unused solar heat decreases from 3.1575 to 3.1213 MWh year^{-1}, representing a reduction of 1.15%, while electrical backup consumption decreased by 6.39%, from 0.3724 to 0.3486 MWh year^{-1}.

Table 4. Effect of Phase Change Material (PCM) location on annual energy performance

Configuration	Solar Fraction at Generator Level [%]	Increase in Solar Fraction [Percentage Points]	Unused Solar Heat [MWh/Year] (Reduction [%])	Electrical Backup [MWh/Year] (Reduction [%])
Without PCM	94.637	Reference	3.1575 (Reference)	0.3724 (Reference)
PCM in collectors only	94.979	+0.342	3.1213 (−1.15%)	0.3486 (−6.39%)
PCM in tank only	94.944	+0.307	3.1393 (−0.58%)	0.3511 (−5.72%)
PCM in collectors and tank	95.263	+0.626	3.1054 (−1.65%)	0.3289 (−11.68%)

Note: The electrical backup consumption reported in Table 4 (0.3289 MWh year^{-1}) corresponds to approximately 0.322 MWh year^{-1} of useful auxiliary thermal input reported in Table 3, considering a heater efficiency of 0.98.

The tank-only configuration produces a comparable but slightly smaller improvement. The generator-level solar fraction reached 94.944%, representing an increase of 0.307 percentage points relative to the reference case. Unused solar heat was reduced by 0.58%, while electrical backup demand decreased by 5.72%. Although the difference between the two single-location configurations was limited, the annual results suggest that collector-integrated PCM provided a marginally greater benefit. This behavior may be associated with its ability to absorb short-duration thermal surpluses close to the collection stage and release them when solar input temporarily decreases. However, confirmation of this mechanism would require a time-resolved analysis of the PCM liquid fraction, collector outlet temperature, and thermal stratification within the storage tank.

The combined configuration achieved the best annual energy performance. The solar fraction at the generator level increased to 95.263%, while unused solar heat and electrical backup decreased to 3.1054 and 0.3289-MWh year^{-1}, respectively. Compared with the PCM-free configuration, these values correspond to reductions of 1.65% in unused solar heat and approximately 11.68% in electrical backup consumption. In absolute terms, the combined arrangement recovered approximately 0.0521 MWh year^{-1} of solar heat that would otherwise remain unused and avoids about 0.0435 MWh year^{-1} of electrical backup energy.

The reduction in electrical backup demand is qualitatively consistent with the experimental findings of Darwesh et al. [34], who observed shorter electric-heater operating periods after incorporating encapsulated RT42 paraffin into a water–PCM storage tank. This agreement supported the interpretation that PCM mainly improves the temporal management and recovery of stored solar heat. However, a direct quantitative comparison is not appropriate because their investigation concerned a flat-plate solar water-heating system operating with RT42 at relatively low temperatures, whereas the present system combines evacuated-tube collectors with RT82 selected for the 75–95 °C operating range of the absorption generator.

The increase of 0.626 percentage points obtained with the combined configuration was slightly lower than the sum of the individual improvements achieved with collector PCM and tank PCM, which amounts to 0.649 percentage points. This result indicated that the two PCM locations provide largely complementary effects, although a small degree of functional overlap existed. The response should therefore not be described as strictly additive or strongly synergistic.

The relatively moderate increase in solar fraction was mainly explained by the already high value of 94.637% obtained by the reference system. Since only 5.363% of the generator demand remained to be supplied by auxiliary energy, the potential for further improvement is inherently limited. Consequently, the benefit of PCM was more clearly reflected in the reduction of electrical backup demand than in the absolute increase in solar fraction.

Overall, PCM integration did not increase the COP or cooling capacity of the absorption machine under the simulated conditions. Instead, it improves the temporal matching between solar energy availability and generator heat demand, reduced unused solar energy, and limits dependence on auxiliary heating. The combined installation of PCM in both the collectors and the storage tank provided the most favourable energy-management performance, while the collector-only configuration appeared slightly more effective than the tank-only arrangement.

3.8 Limitations and uncertainties

Several assumptions should be considered when interpreting the results. The continuous enthalpy formulation captures PCM melting over a finite temperature range but does not explicitly represent supercooling, thermal hysteresis, internal temperature gradients, or long-term degradation [12, 18, 19]. The one-dimensional 20-node tank model reproduces overall thermal stratification while simplifying inlet jets, multidimensional circulation, and local mixing [20, 21]. Collector performance is based on fixed optical and heat-loss coefficients, without explicitly accounting for incidence-angle, wind, fouling, or flow-distribution effects. Long-term changes in vacuum integrity, selective-coating performance, tube ageing, and collector-integrated PCM properties were also neglected. These durability effects, together with the limited availability of long-term experimental validation, remain relevant uncertainties in the assessment of PCM-assisted evacuated-tube collectors [7].

The reduced-order LiBr–H_2O model neglects detailed solution dynamics and start-up and shutdown transients; experimental studies therefore remain necessary for validation [8, 14, 15]. Hourly Meteonorm TMY data represent typical conditions but not sub-hourly variations or exceptional weather years. Cold-room parameters and operating schedules also require sensitivity analysis and experimental calibration [25, 26]. Consequently, the results are suitable for comparing the four configurations, whereas the absolute performance values should be confirmed experimentally.

4. CONCLUSION

This study assessed the annual performance of a solar-assisted absorption refrigeration system combining evacuated-tube collectors, PCM, a stratified thermal storage tank, and a single-effect LiBr–H_2O absorption chiller for a 50 m³ food-storage cold room in Constantine, Algeria. The developed transient model enabled the evaluation of the annual energy balance, the thermal behavior of the main components, and the individual and combined effects of PCM integration under identical climatic, operating, and control conditions.

The combined PCM configuration achieved an annual thermal COP of 0.727 and a thermal solar fraction of 95.263% at the absorption-chiller generator level. This value indicates that solar heat covered most of the annual thermal demand of the generator, while auxiliary heating supplied the remaining fraction. The generator-level solar fraction excludes the electricity consumed by the backup heater and auxiliary components and should therefore not be interpreted as complete energy autonomy of the overall system.

The proposed system maintained the cold room air temperature between approximately 4.10 and 5.60 °C throughout the simulated year, resulting in 100% compliance with the selected product-specific temperature interval of 3–8 °C and no unmet cooling demand. These results indicate that the complete hybrid system maintained the selected product-specific temperature interval throughout the simulated year. However, this temperature-compliance indicator represents conformity with the selected storage interval and should not be considered equivalent to complete HACCP certification.

The four-case comparison showed that PCM integration mainly improves the management and temporal utilization of solar thermal energy rather than the intrinsic COP or cooling capacity of the absorption machine. The reference configuration without PCM already achieved a thermal solar fraction of 94.637% at the generator level. Integrating PCM into both the collectors and the storage tank increased this value by 0.626 percentage points, reduced unused solar heat by 1.65%, and decreased electrical backup consumption by 11.68%. The collector-only configuration provided a slightly greater improvement than the tank-only configuration, whereas the combined arrangement achieved the most favourable overall energy-management performance.

The increase in solar fraction remained moderate because the reference configuration already supplied most of the generator demand from solar energy, leaving limited potential for further improvement. The results indicate that collector-level and tank-level PCM provide largely complementary thermal-buffering effects, although their combined contribution is not strictly additive. Their main benefit lies in improving the temporal matching between solar availability and generator demand, reducing curtailed solar heat, and limiting dependence on auxiliary heating.

Overall, the proposed configuration appears thermodynamically feasible for solar-assisted food refrigeration under the simulated climatic and operating conditions. Future investigations should include experimental validation, the use of measured or independently validated weather data, and sensitivity analyses of PCM mass, phase-change temperature, collector area, storage volume, and control parameters. Economic and environmental assessments are also required to determine whether the achieved reduction in auxiliary-energy consumption justifies the additional cost and complexity associated with PCM integration.

REFERENCES

[1] International Energy Agency (IEA). (2023). Space cooling. Net Zero Emissions Guide. IEA, Paris, France. https://www.iea.org/reports/space-cooling-2.

[2] Ketfi, O., Merzouk, M., Kasbadji Merzouk, N., El Metenani, S. (2015). Performance of a single effect solar absorption cooling system (LiBr-H2O). Energy Procedia, 74: 130-138. https://doi.org/10.1016/j.egypro.2015.07.534

[3] Al-Falahi, A., Alobaid, F., Epple, B. (2020). A new design of an integrated solar absorption cooling system driven by an evacuated tube collector: A case study for Baghdad, Iraq. Applied Sciences, 10(10): 3622. https://doi.org/10.3390/app10103622

[4] Gomri, R. (2013). Simulation study on the performance of solar/natural gas absorption cooling chillers. Energy Conversion and Management, 65: 675-681. https://doi.org/10.1016/j.enconman.2011.10.030

[5] Marashli, A., Alfanatseh, E., Shalby, M., Gomaa, M.R. (2022). Modelling single-effect of lithium bromide-water (LiBr-H2O) driven by an evacuated solar tube collector in Ma'an city (Jordan) case study. Case Studies in Thermal Engineering, 37: 102239. https://doi.org/10.1016/j.csite.2022.102239

[6] Kumar, A., Said, Z., Bellos, E. (2021). An up-to-date review on evacuated tube solar collectors. Journal of Thermal Analysis and Calorimetry, 145(6): 2873-2889. https://doi.org/10.1007/s10973-020-09953-9

[7] Jaber, H.S., Khalaf, B.S. (2025). A comprehensive review of evacuated tube solar collectors: Advances in design, simulation, and applications. International Journal of Heat and Technology, 43(5): 1927-1938. https://doi.org/10.18280/ijht.430532

[8] Boero, A., Agyenim, F. (2020). Modeling and simulation of a small-scale solar-powered absorption cooling system in three cities with a tropical climate. International Journal of Low-Carbon Technologies, 15(1): 1-16. https://doi.org/10.1093/ijlct/ctz040

[9] Redpath, D., Paneri, A., Singh, H., Ghitas, A., Sabry, M. (2022). Design of a building-scale space solar cooling system using TRNSYS. Sustainability, 14(18): 11549. https://doi.org/10.3390/su141811549

[10] Zheng, L., Zhang, W., Liang, F. (2017). A review about phase change material cold storage system applied to solar-powered air-conditioning system. Advances in Mechanical Engineering, 9(6): 1-20. https://doi.org/10.1177/1687814017705844

[11] Mehmood, S., Lizana, J., Friedrich, D. (2023). Solar-driven absorption cooling system with latent heat storage for extremely hot climates. Energy Conversion and Management, 297: 117737. https://doi.org/10.1016/j.enconman.2023.117737

[12] Papadimitratos, A., Sobhansarbandi, S., Pozdin, V., Zakhidov, A., Hassanipour, F. (2016). Evacuated tube solar collectors integrated with phase change materials. Solar Energy, 129: 10-19. https://doi.org/10.1016/j.solener.2015.12.040

[13] Wang, Z., Zhang, H., Dou, B., Zhang, G., Wu, W., Zhou, L. (2020). An experimental study for the enhancement of stratification in heat-storage tank by equalizer and PCM module. Journal of Energy Storage, 27: 101010. https://doi.org/10.1016/j.est.2019.101010

[14] Guerrero Delgado, M.C., Sanchez Ramos, J., Castro

Medina, D., Palomo Amores, T.R., Cerezo-Narvaez, A., Alvarez Dominguez, S. (2022). Fresnel solar cooling plant for buildings: Optimal operation of an absorption chiller through inverse modelling. Energy Reports, 8: 3189-3212. https://doi.org/10.1016/j.egyr.2022.02.128
[15] Sharma, D.K., Sharma, D., Ali, A.H.H. (2023). Optimization and thermo-economic performance of a solar-powered vapor absorption cooling system integrated with sensible thermal energy storage. Energy Conversion and Management: X, 20: 100440. https://doi.org/10.1016/j.ecmx.2023.100440
[16] Codex Alimentarius Commission. (2022). General Principles of Food Hygiene, CXC 1-1969. FAO and WHO, Rome, Italy. https://www.fao.org/fao-who-codexalimentarius/codex-texts/codes-of-practice/en/.
[17] Ibrahim, N.I., Yahiaoui, A., Garkuwa, J.A., Ben Mansour, R., Rehman, S. (2024). Solar cooling with absorption chillers, thermal energy storage, and control strategies: A review. Journal of Energy Storage, 97: 112762. https://doi.org/10.1016/j.est.2024.112762
[18] Al-Abdali, A.M., Ammari, H. (2022). Thermal energy storage using phase-change material in evacuated-tubes solar collector. AIMS Energy, 10(3): 486-505. https://doi.org/10.3934/energy.2022024
[19] Rubitherm Technologies GmbH. (2020). RT82 Technical Data Sheet, version 09.10.2020. Rubitherm Technologies GmbH, Berlin, Germany.
[20] Karlina, Y., Yerdesh, Y., Toleukhanov, A., Belyayev, Y., Wang, H.S., Botella, O. (2024). Numerical simulation study of thermal performance in hot water storage tanks with external and internal heat exchangers. Energies, 17(22): 5623. https://doi.org/10.3390/en17225623
[21] De la Cruz-Loredo, I., Zinsmeister, D., Licklederer, T., et al. (2023). Experimental validation of a hybrid 1-D multi-node model of a hot water thermal energy storage tank. Applied Energy, 332: 120556. https://doi.org/10.1016/j.apenergy.2022.120556
[22] Patek, J., Klomfar, J. (2006). A computationally effective formulation of the thermodynamic properties of LiBr-H2O solutions from 273 to 500 K over full composition range. International Journal of Refrigeration, 29(4): 566-578. https://doi.org/10.1016/j.ijrefrig.2005.10.007
[23] Kader, A.A., Arpaia, M.L. (1999). Orange: Recommendations for maintaining postharvest quality. Postharvest Research and Extension Center, University of California, Davis, USA. https://postharvest.ucdavis.edu/produce-facts-sheets/orange.
[24] Codex Alimentarius Commission. (2017). Code of Hygienic Practice for Fresh Fruits and Vegetables, CXC 53-2003. FAO and WHO, Rome, Italy. https://www.fao.org/fao-who-codexalimentarius/codex-texts/codes-of-practice/en/.
[25] ASHRAE. (2022). 2022 ASHRAE Handbook-Refrigeration, SI Edition. American Society of Heating, Refrigerating and Air-Conditioning Engineers, Atlanta, GA, USA.
[26] Lanca, M., Garcia, J., Gomes, J. (2025). Heat transfer mechanisms in refrigerated spaces: A comparative study of experiments, CFD predictions and heat load software accuracy. Energies, 18(23): 6280. https://doi.org/10.3390/en18236280
[27] Zhu, H., Guo, B., Geng, W., Chi, J., Guo, S. (2022). Simulation of an improved solar absorption refrigeration system with phase change materials. Energy Reports, 8: 3671-3679. https://doi.org/10.1016/j.egyr.2022.02.306
[28] Li, Q., Zhao, S., Wang, D., et al. (2023). Simulation study on solar single/double-effect switching LiBr-H2O absorption refrigeration system. Energies, 16(7): 3220. https://doi.org/10.3390/en16073220
[29] Mostafa, A., Hassanain, M., Elgendy, E. (2022). Transient simulation and design parameters optimization of a cold store utilizing a solar-assisted adsorption refrigeration system. Case Studies in Thermal Engineering, 37: 102273. https://doi.org/10.1016/j.csite.2022.102273
[30] Alammar, A., Rezk, A., Alaswad, A., Decker, S.D., Ruhumuliza, J., Gasana, Q. (2020). Modelling of cold store for agro-products using solar-driven adsorption chiller under Rwandan environmental conditions. Energy Proceedings, 10. https://doi.org/10.46855/energy-proceedings-7205
[31] Essa, M.A., Rofaiel, I.Y., Ahmed, M.A. (2020). Experimental and theoretical analysis for the performance of evacuated tube collector integrated with helical finned heat pipes using PCM energy storage. Energy, 206: 118166. https://doi.org/10.1016/j.energy.2020.118166
[32] Mercier, S., Villeneuve, S., Mondor, M., Uysal, I. (2017). Time-temperature management along the food cold chain: A review of recent developments. Comprehensive Reviews in Food Science and Food Safety, 16(4): 647-667. https://doi.org/10.1111/1541-4337.12269
[33] James, S.J., James, C. (2010). The food cold-chain and climate change. Food Research International, 43(7): 1944-1956. https://doi.org/10.1016/j.foodres.2010.02.001
[34] Darwesh, B.D., Hamakhan, I.A., Yaqob, B.N. (2022). Thermal enhancement of solar energy storage using phase change materials. International Journal of Heat and Technology, 40(3): 758-766. https://doi.org/10.18280/ijht.400314

NOMENCLATURE

A	Surface area, m²
C	Thermal capacitance, J K⁻¹
c_p	Specific heat capacity, J·kg⁻¹·K⁻¹
E	Annual energy, MWh year⁻¹
f	PCM liquid fraction
G_β	Solar irradiance on the tilted collector, W·m⁻²
H	Nodal enthalpy, J
L	Latent heat of fusion, J·kg⁻¹
m	Mass, kg
$\dot{Q}$	Thermal power or heat-transfer rate, W
$R_{3\text{–}8}$	Temperature-compliance rate within 3–8 °C, %
SF	Thermal solar fraction, %
T	Temperature, ℃ or K
U / UA	Heat-transfer coefficient / thermal conductance, W·m⁻²·K⁻¹ / W·K⁻¹
V	Volume, m³ or L

Greek symbols

β	Collector tilt angle, °

η	Efficiency or utilization ratio, %
η_o	Collector optical efficiency
ΔT	Temperature difference or phase-change interval, K

Abbreviations

COP	Coefficient of performance
ETC	Evacuated Tube Collector
HACCP	Hazard Analysis and Critical Control Points
$LiBr–H_2O$	Lithium bromide–water working pair
NR	Not reported
PCM	Phase Change Material
PLR	Part-load ratio
TMY	Typical Meteorological Year

Subscripts

air, p, w, pcm	Air, stored product, water, and phase change material
aux, solar	Auxiliary and solar energy sources
coll, tank, gen, cool	Collector, storage tank, generator, and cooling subsystem
in, out, ext, int	Inlet, outlet, external, and internal
tr, leak, door, prod	Transmission, leakage, door-opening, and product loads
min, max, nom	Minimum, maximum, and nominal values
req, cmd, avail, cap	Required, commanded, available, and capacity-corrected values
hyd, inter, loss	Hydraulic transfer, inter-nodal transfer, and thermal loss
ref, th, total	Reference, thermal, and total values